Journal of Materials Chemistry A

PAPER

View Article Online
View Journal | View Issue

Cite this: J. Mater. Chem. A, 2017, 5, 7912

Redox chemistry of $CaMnO_3$ and $Ca_{0.8}Sr_{0.2}MnO_3$ oxygen storage perovskites†

B. Bulfin,*[a] J. Vieten,[a] D. E. Starr,[c] A. Azarpira,[c] C. Zachäus,[c] M. Hävecker,[d] K. Skorupska,[d] M. Schmücker,[b] M. Roeb[a] and C. Sattler[a]

Received 24th January 2017
Accepted 19th March 2017

DOI: 10.1039/c7ta00822h

rsc.li/materials-a

Perovskite oxides $CaMnO_3$ and $Ca_{0.8}Sr_{0.2}MnO_3$ show continuous non-stoichiometry over a range of temperatures and oxygen partial pressures. In this work a thermobalance equipped with an oxygen pump was used to measure the equilibrium non-stoichiometry of both materials for temperatures in the range 400–1200 °C and oxygen partial pressures in the range 1–10^{-5} bar. Analysis of the data showed that $Ca_{0.8}Sr_{0.2}MnO_3$ has a lower enthalpy of reduction and thus can be more easily reduced. The strontium added sample was also robust against a phase transition that was seen in $CaMnO_3$ at high temperatures. A statistical thermodynamic model of the system suggests that the defects form clusters of the form $(Mn'_{Mn}V_O^{\cdot\cdot}Mn'_{Mn})^{\times}$. The oxidation kinetics were also investigated with $Ca_{0.8}Sr_{0.2}MnO_3$ showing faster kinetics and maintaining activity at lower temperatures. Overall, $Ca_{0.8}Sr_{0.2}MnO_3$ shows very promising properties for redox applications, including gravimetric oxygen storage up to 4% by mass, high stability and rapid reversibility, with re-oxidation in less than 1 min at 400 °C. Finally, the redox chemistry of $Ca_{0.8}Sr_{0.2}MnO_3$ was also investigated using *in situ* X-ray photoelectron spectroscopy and near-edge X-ray absorption measurements at near ambient pressure in oxygen atmospheres.

Introduction

Metal oxides featuring multivalent species are highly valuable for applications as redox materials. The combination of a high temperature step, at which the oxide is partially reduced under the release of oxygen gas, and a low temperature oxidation step is referred to as a thermochemical cycle.[1] The metal oxide ideally is not degraded and can be recycled between the different oxidation steps. Thermochemical cycles can be applied for H_2O or CO_2 splitting,[2–4] for combustion of organic fuels,[5] or for oxygen storage and air separation.[6] Besides binary oxide systems such as CuO/Cu_2O or CoO/Co_3O_4,[6,7] perovskite materials with the general formula AMO_3 are a promising alternative.[8] Typically, the A site features an alkali, alkaline earth or rare earth metal cation, whereas the M site is occupied in most cases by transition metal cations. The occurrence of an oxygen non-stoichiometry δ ($\delta = 0$–0.5) in $AMO_{3-\delta}$ perovskites, as well as the close structural relationship between perovskites and their defect-ordered reduced form $A_2M_2O_5$ (brownmillerite) allow for fast redox kinetics.[9]

$$AMO_3 \overset{T,p_{O_2}}{\longleftrightarrow} AMO_{3-\delta} + \frac{\delta}{2}O_2, \quad (1)$$

We recently reported the synthesis of various perovskite materials and their application for air separation and oxygen storage. Out of all materials we investigated, $Ca_{0.8}Sr_{0.2}MnO_3$ showed the highest gravimetric oxygen storage capacity, whereas $CaMnO_3$ featured the highest redox mass change per Kelvin of temperature change in the studied temperature regime.[10] The synthesis of both materials has been reported in the literature.[11–13] Moreover, the redox properties and enthalpies of $CaMnO_3$ and calcium containing perovskites have been studied before.[11,12,14–16] In this work, we study the redox properties of both materials, determining their partial molar entropy Δh° and entropy Δs° of the reduction by observing redox equilibria at different oxygen partial pressures and temperatures. We also compare the stability and reaction kinetics of $Ca_{0.8}Sr_{0.2}MnO_3$ to those of the strontium free perovskite $CaMnO_3$.

Theory

In order to theoretically describe the partial reduction of perovskites, we consider the complete reduction reaction

$$2AMO_3 \rightarrow 2AMO_{2.5} + \frac{1}{2}O_2. \quad (2)$$

[a]Institute of Solar Research, German Aerospace Center, 51147 Cologne, Germany. E-mail: brendan.bulfin@dlr.de; Tel: +49 (0)2203 6014130
[b]Institute of Materials Research, German Aerospace Center, 51147 Cologne, Germany
[c]Institute of Solar Fuels, Helmholtz-Zentrum Berlin für Materialien und Energie GmbH, Hahn-Meitner-Platz 1, 14109 Berlin, Germany
[d]Department of Inorganic Chemistry, Fritz Haber Institute of the Max Plank Society, Faradayweg 4-6, 14195 Berlin, Germany

† Electronic supplementary information (ESI) available. See DOI: 10.1039/c7ta00822h

Assuming that doubly ionized oxygen vacancies are formed, this reduction reaction can then be written in Kröger–Vink notation as

$$O_O^{\times} + 2M_M^{\times} = V_O^{\cdot\cdot} + 2M_M^{'} + \frac{1}{2}O_2, \quad (3)$$

where the products can also form defect clusters like $(M_M^{'}V_O^{\cdot\cdot}M_M^{'})^{\times}$.

The unit-less vacancy concentration δ is defined as

$$\delta = \frac{[V_O^{\cdot\cdot}]}{[A]}, \quad (4)$$

where the oxygen vacancy concentration $[V_O^{\cdot\cdot}]$ is normalised with respect to the concentration of A site ions [A], which is constant. Similarly the unit-less concentration of oxygen which can be removed from the lattice is given by

$$0.5 - \delta = \frac{[O_O^{\times}]}{[A]}, \quad (5)$$

where $[O_O^{\times}]$ only corresponds to the concentration of removable oxygen.

The equilibrium equations for the reduction reaction are

$$\Delta g_{\delta} = \Delta g_{\delta}^{\circ} + \frac{1}{2}RT\ln\left(\frac{p_{O_2}}{p^{\circ}}\right) = 0, \quad (6)$$

$$\Delta g_{\delta}^{\circ} = \Delta h_{\delta}^{\circ} - T\Delta s_{\delta}^{\circ}. \quad (7)$$

where the subscript δ indicates that they are partial molar quantities $\Delta g_{\delta} = \frac{\partial \Delta g}{\partial \delta}$, and the superscript $^{\circ}$ indicates that the value is at standard pressure, $\Delta g_{\delta}^{\circ}$. If the partial molar enthalpy change $\Delta h_{\delta}^{\circ}$, and entropy $\Delta s_{\delta}^{\circ}$ are determined, then eqn (6) and (7) give an equation of state.

For the reaction given in eqn (2), the change in entropy to produce δ oxygen vacancies starting from AMO_3 is given by

$$\Delta s_{vac}^{\circ} = \delta\Delta s_{th}^{\circ} + \Delta s_{con}. \quad (8)$$

The thermal entropy change Δs_{th}° is the entropy of oxygen gas and change in the lattice vibrational entropy caused by introducing vacancies

$$\Delta s_{th}^{\circ} = \frac{1}{2}s_{O_2}^{\circ} + \Delta s_{v}^{\circ}. \quad (9)$$

The configurational entropy is taken from the previous derivation by the authors for ceria,[17] and is given by

$$\Delta s_{con} = aR(x\ln(x) + (1 - x)\mathrm{In}(1 - x)), \quad (10)$$

where x is the mole fraction of vacancies given by $\frac{\delta}{0.5}$. This term is essentially an entropy of mixing dependence, where the value of a determines the number of moles which are being mixed. If no defect clusters form, we have 1 mole of $V_O^{\cdot\cdot}$ defects and 2 moles of $M_M^{'}$ defects giving a total of 3, and so $a = 3$. On the other hand, $a = 1$ corresponds to an entropy of mixing for just 1 mole, and so all defects must be forming clusters of the form $(M_M^{'}V_O^{\cdot\cdot}M_M^{'})^{\times}$. In this way, a can be set as a free parameter with its fit value indicating the degrees of freedom of the defects. A value of $a < 1$ would indicate that there is some additional ordering of defects, which is the case in a number of other perovskite oxides.[9,18]

Finally, in order to obtain the partial molar entropy we must take the derivative of eqn (10) with respect to the vacancy concentration δ, giving

$$\Delta s_{\delta}^{\circ}(\delta) = \frac{\partial \Delta s_{vac}}{\partial \delta} = \Delta s_{th} + 2aR(\ln(0.5 - \delta) - \ln(\delta)). \quad (11)$$

Combining eqn (11) for the partial molar entropy with eqn (6) and (7) gives an equation of state

$$\left(\frac{\delta}{0.5 - \delta}\right)^{2a} = \left(\frac{p_{O_2}}{p^{\circ}}\right)^{-\frac{1}{2}}\exp\left(\frac{\Delta s_{th}}{R}\right)\exp\left(\frac{-\Delta h_{\delta}^{\circ}}{RT}\right). \quad (12)$$

In some cases, it is also necessary to include a dependence of $\Delta h_{\delta}^{\circ}$ on δ and temperature,[17,19] but as we shall see later, a constant value offers a very good fit for the materials studied here.

Results and discussion

The XRD patterns of the prepared $CaMnO_3$ and $Ca_{0.8}Sr_{0.2}MnO_3$ perovskites confirming the phase formation are given in the ESI† along with EDX and XPS measurements confirming the composition of the $Ca_{0.8}Sr_{0.2}MnO_3$ sample.

Thermodynamics

The entire TGA datasets used to characterize the redox thermodynamics are also given in Fig. 1 in the ESI.† From this, one immediate difference between the two materials is that $CaMnO_3$ is seen to decompose at high temperature and low oxygen partial pressure, which is in agreement with a previous study on $CaMnO_3$.[12]

In order to determine the resulting compounds after the decomposition, it was repeated without recovering the perovskite (see ESI†). The produced powder was then subjected to XRD analysis, which showed that the transition resulted in a mixture of calcium manganese oxide Ca_2MnO_4/2CaOMnO$_2$ and Marokite $CaMn_2O_4$, which is in agreement with the previous work of Bakken *et al.*[11] After the decomposition, the reformation of the perovskite required heating to high temperature under high oxygen partial pressure. The decomposition re-occurred during the next reduction phase (Fig. 1 in the ESI†). The decomposition is due to the decreasing stability of the oxides with increasing oxygen non-stoichiometry and it appears to take place for mass changes in the region $\Delta m = 2.5$–3%, or $\delta \approx 0.23$–0.26 in $CaMnO_{3-\delta}$.

This decomposition was not observed in $Ca_{0.8}Sr_{0.2}MnO_3$, which may be a result of the higher ionic radius of Sr^{2+} balancing out the increased ionic radius of Mn^{3+}, with respect to Mn^{4+}, thus stabilizing the perovskite. The Goldschmidt tolerance factor is a viable measure to determine the stability of

perovskites.[13] $CaMnO_3$ has a tolerance slightly less than 1.00, and $Ca_{0.8}Sr_{0.2}MnO_3$ has a tolerance factor slightly greater than 1.00. Upon reduction, the tolerance factor decreases due to the increased radius of the reduced metal cations. This can lead to a distortion and eventually decomposition of the perovskite structure, which can be avoided by increasing the initial tolerance factor.

The fact that $CaMnO_3$ decomposed means that it is not suitable for the strong reducing environments present in chemical looping combustion (CLC). In order to address this, Pishahang *et al.* used $CaMn_{0.5}Ti_{0.5}O_3$,[20] where the titanium helps to make the material more robust, but also decreases the oxygen storage capacity. $Ca_{0.8}Sr_{0.2}MnO_3$ appears to be robust against decomposition, and mass changes up to $\Delta m = 4\%$ were easily reversible. Therefore, it may offer an excellent material for chemical looping combustion with a larger oxygen storage capacity than $CaMn_{0.5}Ti_{0.5}O_3$. This has also been noted by Galinsky *et al.*,[21] who found that $Ca_{0.75}Sr_{0.25}MnO_3$ was also more stable under reducing conditions than $CaMnO_3$, and they suggested that it is an excellent candidate material for chemical looping combustion with oxygen uncoupling. This is a recent idea proposed as an alternative to chemical looping combustion, that can be used with solid fuels,[22] where gaseous oxygen must be released by the oxide for combustion of the solid fuel, as opposed to the oxide reacting directly with the fuel.

The non-stoichiometry value δ can be calculated from the mass changes measured in the TGA using the formula

$$\delta = \frac{\Delta m}{m}\frac{M_{\text{sample}}}{M_{\text{O}}}, \tag{13}$$

where m is the sample mass, M_{O} is the molar mass of molecular oxygen and M_{sample} is the molar mass of the sample. The absolute δ value is obtained by assuming that the initial oxidised sample has a vacancy concentration of $\delta = 0$.

Equilibrium points were extracted from the raw TGA data in the figure (ESI†), by selecting the plateau regions where Δm, T and p_{O_2} are all approximately constant with respect to time. These extracted equilibrium values are shown in the top section of Fig. 1, where no data points were taken after the phase transition seen for $CaMnO_3$. It can be seen here that for lower temperatures and higher partial pressures, $Ca_{0.8}Sr_{0.2}MnO_3$ shows a larger reduction extent δ than $CaMnO_3$. Under the most reducing conditions, before $CaMnO_3$ decomposes, they show a similar non-stoichiometry δ. To better understand this result, we can look at the intrinsic thermodynamic properties of the materials.

The partial molar enthalpy and entropy for a given δ value can be determined from this experimental dataset. To understand this, one should note that eqn (6) and (7) give the condition

$$\frac{1}{2}\ln\left(\frac{p_{O_2}}{p^\circ}\right) = \frac{-\Delta h^\circ_\delta}{RT} + \frac{\Delta s^\circ_\delta}{R}\bigg|_{\delta=\text{const}}. \tag{14}$$

Therefore, plots of $\frac{1}{2}\ln(p_{O_2})$ *vs.* $\frac{-1}{RT}$ for a given value of δ should give Δh°_δ as the slope and $\frac{\Delta s^\circ_\delta}{R}$ as the intercept. To obtain the data at constant δ required for these plots, the experimental data were interpolated between data points. Note that none of the points were obtained by extrapolating.

These extracted thermodynamic values are shown in the lower section of Fig. 1, The data for $CaMnO_3$ are in good agreement with the work of Rørmark *et al.*[12] The most noticeable difference between the materials is that $Ca_{0.8}Sr_{0.2}MnO_3$ has a lower enthalpy of reaction compared to $CaMnO_3$, but also a slightly lower entropy of reduction. A DFT study by Curnan and Kitchin suggests that the energy of formation of oxygen vacancies in perovskites with an ideal cubic structure is lower compared to orthorhombic and rhombohedral distorted perovskites.[23] The lower enthalpy of reduction for $Ca_{0.8}Sr_{0.2}MnO_3$ may then be explained by Sr increasing the tolerance factor, and decreasing the distortion of the cubic structure in the reduced perovskite.

The lower enthalpy of reduction explains why $Ca_{0.8}Sr_{0.2}MnO_3$ has a slightly higher reduction extent at lower temperatures, but at higher temperatures the larger entropy change for $CaMnO_3$ means that they have similar reduction extents.

Finally, the model given in eqn (12) was fit to the data with the result also plotted in each section of Fig. 1. The values of the fits are shown in Table 1. In the case of $Ca_{0.8}Sr_{0.2}MnO_3$, the model works very well and the value of the parameter a was very close to 1, indicating that most of the defects form clusters of the form $(M'_M V^{\cdot\cdot}_O M'_M)^\times$. This model fit offers physical insight and a valuable tool for analysis and simulation work.

The decomposition that occurred during the reduction of $CaMnO_3$ means that a smaller range of data was available, resulting in larger errors in the fit parameters. In addition, the value of a was found to be less than one. This would suggest that there is some additional vacancy ordering besides the formation of $Mn^{3+}V^{\cdot\cdot}_O Mn^{3+}$ defect clusters, which is expected according to Reller *et al.*[24] At lower temperatures, the model overestimates the values of δ, which can be explained by the fact that the additional vacancy ordering is more predominant at lower temperatures.[25]

An interesting point worth noting is that in a perovskite the oxygen has two fold co-ordination with the Mn^{4+} sites. This means that there is only one way to configure $(M'_M V^{\cdot\cdot}_O M'_M)^\times$ defect clusters. In contrast, in the ceria fluorite structure, oxygen has a 4-fold co-ordination with Ce^{4+} sites and thus there is freedom in the configuration of individual defect associations. Moreover, there are DFT studies which suggest that defect clusters prefer the next nearest neighbour ceria sites,[26,27] leading to a lot of possible configurations, which would explain the much larger entropy of defect formation seen in ceria compared to perovskites.[17] This is a fundamental limitation of the crystal motifs of these materials, and thus perovskite oxides, regardless of composition, will likely have a lower entropy of vacancy formation than ceria. This has important implications for designing materials for thermochemical fuel production cycles, where perovskites[28,29] have been suggested as a lower temperature alternative to the ceria cycle.[30] In this particular application, the oxide must have a large enough enthalpy of reduction Δh° to reduce steam or carbon dioxide (>300 kJ mol^{-1}). From eqn (7), we see that the change in entropy is the

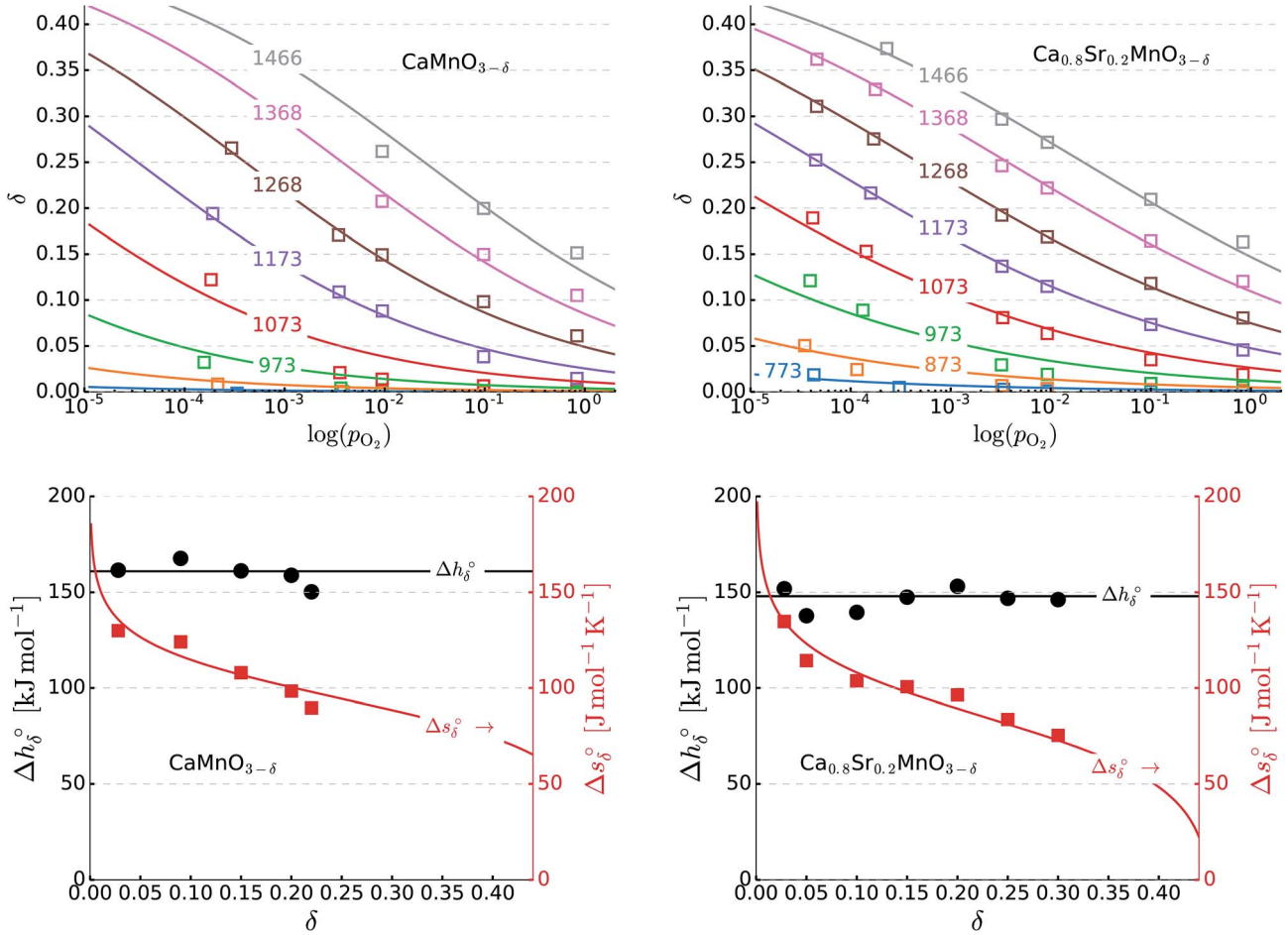

Fig. 1 Above: Equilibrium oxygen vacancy concentration δ values *vs.* p_{O_2}, experimental data points plotted along with the fit (lines) of eqn (12) and in-graph labels giving the temperatures in Kelvin, for both $CaMnO_3$ and $Ca_{0.8}Sr_{0.2}MnO_3$. The data for $CaMnO_3$ stop at a lower δ value due to the phase change which occurred during reduction. Below: Values of partial molar enthalpy Δh_δ° and entropy Δs_δ°, determined from the experimental data as well as the model fits.

driving force for the reduction reaction, and so perovskites have a lower driving force than ceria based materials. Thus, for a given enthalpy, perovskites require higher temperatures for the reduction reaction to proceed than a ceria-based material. It is, therefore, likely to be quite difficult to produce a perovskite which is significantly better than ceria for this application.

Kinetics

The oxidation kinetics at temperatures in the range of 200–500 °C were investigated for both materials. The $Ca_{0.8}Sr_{0.2}MnO_3$ sample was reduced under argon at 900 °C, and $CaMnO_3$ was reduced at 900 °C in a mixture of argon and synthetic air with $p_{O_2} = 0.004$ bar. This was to avoid decomposition (see Fig. 1 in the ESI†).

In both cases, there was some variance in the absolute δ value at the start of reduction, due to varying degrees of re-oxidation during the cool down. For that reason, the fraction complete is plotted in Fig. 2, rather than the actual δ values. At the start of reduction in each case $\delta > 0.1$, and was closer to 0.2 in the case of $Ca_{0.8}Sr_{0.2}MnO_3$.

In Fig. 2, it can be seen that $Ca_{0.8}Sr_{0.2}MnO_3$ exhibits faster kinetics and also maintains a high activity down to lower temperatures. At temperatures as low as 350 °C, $Ca_{0.8}Sr_{0.2}MnO_3$ shows complete re-oxidation after just 5 min. $CaMnO_3$, on the other hand, requires 30 min for the reaction to be halfway to completion at the same temperature. Fast kinetics mean that the materials can be quickly cycled from the reduced to oxidised state, which is very promising for oxygen storage and oxygen pumping applications, such as thermochemical air separation.

After the kinetic analysis, SEM images of the powders were taken, to see if there was any difference in the morphology between the two samples. There was no noticeable difference and so the difference in kinetics between the two materials

Table 1 Fit parameters of the model given in eqn (12). The error in enthalpy is the standard deviation of the values, and for a and Δs_{th} it was taken from the square root of the covariance matrix for the fit

	Δh_δ° [kJ mol^{-1}]	a [–]	Δs_{th} [J K^{-1}mol^{-1}]
$CaMnO_3$	161 ± 6	0.88 ± 0.04	94 ± 7
$Ca_{0.8}Sr_{0.2}MnO_3$	148 ± 5	1.10 ± 0.03	85 ± 3

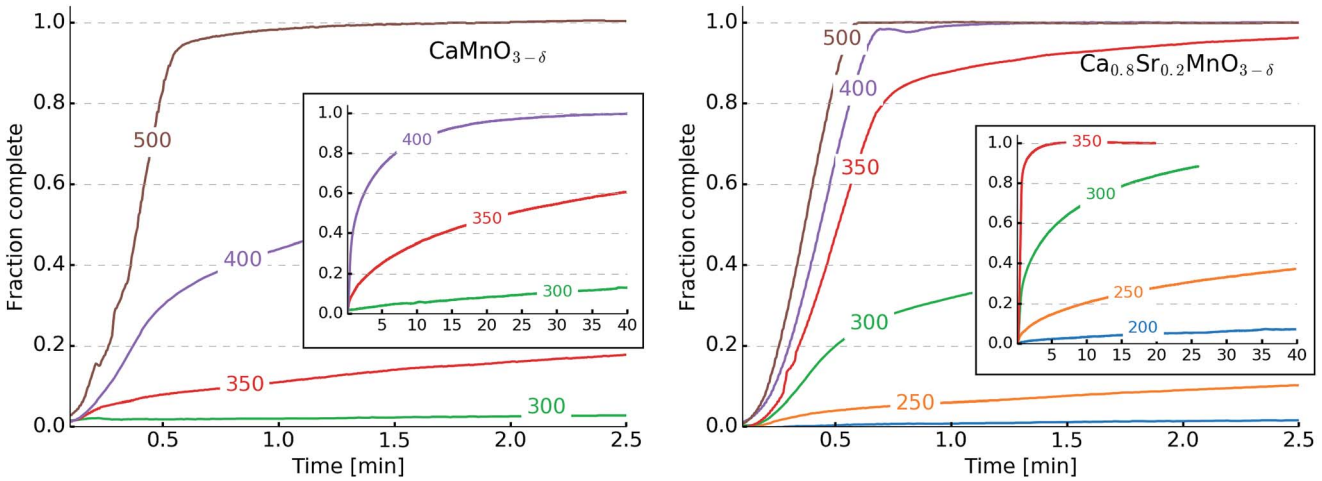

Fig. 2 Re-oxidation kinetics plotted as fraction complete *vs.* time for both $CaMnO_3$ and $Ca_{0.8}Sr_{0.2}MnO_3$ with the temperature at which the reaction is taken place marked on each line in Celsius. The inset graphs show the lower temperature kinetics over a 40 minute period. For the fraction complete, the value 1.0 corresponds to total re-oxidation to $CaMnO_3$.

must be a result of the intrinsic transport properties, such as oxygen ion mobility and surface exchange rates. One explanation for the improved kinetics is that the $Ca_{0.8}Sr_{0.2}MnO_3$, maintains a better cubic structure when reduced, which would offer better diffusion pathways for the oxide ions and increase the oxygen ion mobility.

It should be noted that at the high temperatures required for reduction the kinetics seemed only to be limited by the constraints of the TGA: heating rates and gas flow rates.

X-ray spectroscopy

The reduction and re-oxidation of $Ca_{0.8}Sr_{0.2}MnO_{3-\delta}$ were observed *in situ* at near ambient pressure *via* X-ray photoelectron spectroscopy (NAP-XPS),[31] and near edge absorption spectroscopy (NEXAFS), using the ISISS beamline synchrotron, Berlin. Using NEXAFS, Mn^{3+} and Mn^{4+} species could be distinguished by measuring the absorption at the Mn L edge (see Fig. 3). With increasing temperature, and/or decreasing oxygen partial pressure, the Mn^{3+} signal (dominant at energies of approximately E_{exc} = 641.5 eV) increased in intensity with respect to the Mn^{4+} signal, which is dominant at higher energies of around 643.5 eV.[32]

This is in good agreement with the expected reduction of the perovskite under these conditions (see Fig. 2). The measurement at 400 °C and 1 mbar O_2 partial pressure was carried out after previous reduction at 700 °C and low oxygen pressure of 7.5×10^{-4} mbar, showing the reversibility of the reduction and the successful re-oxidation of the perovskite under these conditions.

The XPS spectra of the elements Ca, Sr, Mn and O were also recorded both under vacuum at room temperature, and at high temperatures (400–700 °C) and varying oxygen partial pressures. These scans as well as full spectrum survey scans can be seen in the ESI.† Carbonaceous species, most probably carbonates, were observed in the loaded samples, which could be easily removed by initial heating to T > 300–500 °C in oxygen. The Ca 2p and Sr 3d peaks showed no significant changes in the shape or position upon reduction, as expected. Moreover, the Mn 2p also showed only little changes in the position, and therefore, NEXAFS as a more sensitive method was chosen to illustrate the change in the oxidation state of the Mn cations. The most dramatic change in the shape and intensities upon reduction was observed for the O 1s spectra, as shown in Fig. 4.

Three distinct oxygen species are observed as can be seen from the fits shown in Fig. 4. The data were very well fit using Gaussians and by fixing the relative distances between the peaks to be the same in all cases, which allows for inaccuracies

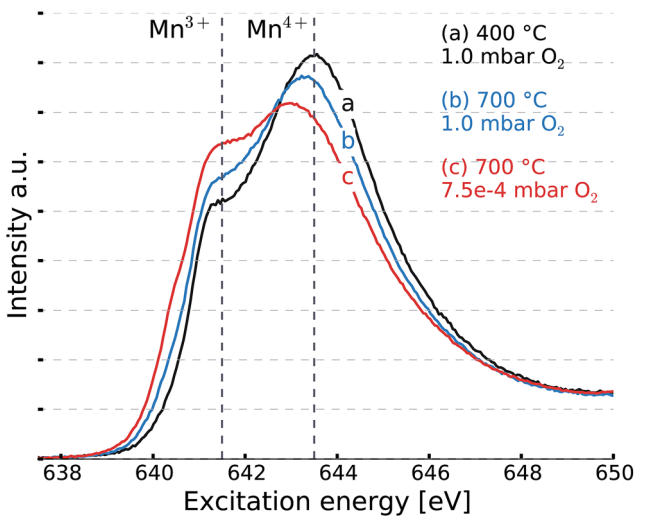

Fig. 3 NEXAFS scan of the Mn L edge at different temperatures and oxygen partial pressures, where the intensities have been normalized by peak areas and the excitation energy was calibrated using a standard peak feature in the mirror current. With increasing temperature and/or decreasing oxygen partial pressure, the reduction proceeds, which is indicated by an increase of the Mn^{3+} absorption intensity with respect to Mn^{4+}. Spin–orbit splitting causes the appearance of a second set of peaks at higher photon energy.

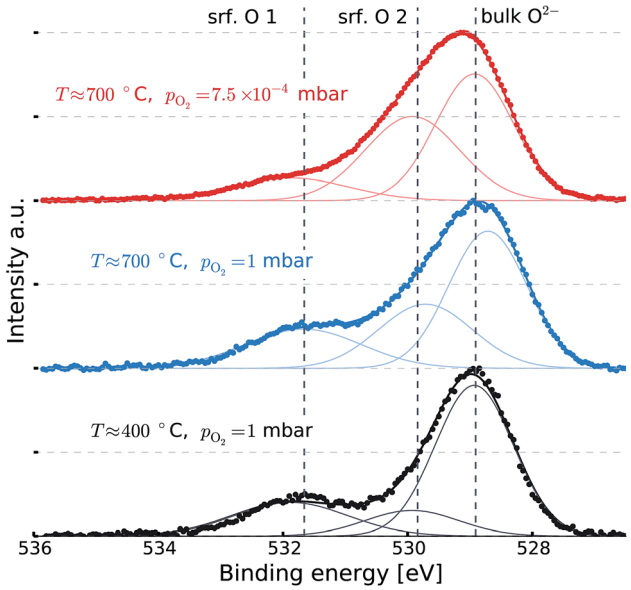

Fig. 4 XPS of the O 1s peaks at different temperatures and partial pressures. Under reducing conditions, the surface oxygen peak (srf. O 1) can be seen to decrease relative to the bulk.

in the set excitation beam energy. The one at the lowest 1s binding energy (BE) of approximately 529.0 eV is assigned to bulk lattice oxide ions (O^{2-}). This peak intensity showed an increasing trend with increasing excitation energy (see Fig. 5), corresponding to a greater depth, according to the universal curve of inelastic scattering in solids,[33] which confirms that these species are located mainly in the sub-surface layers of the perovskite. This result is in good agreement with data by Crumlin *et al.* for a similar perovskite.[34]

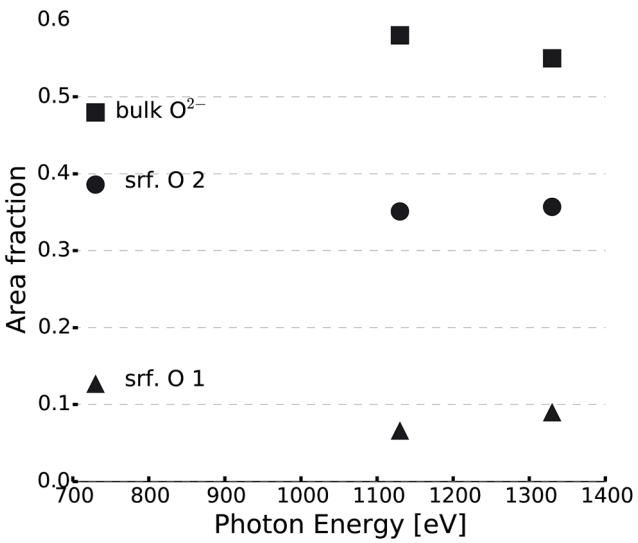

Fig. 5 Relative intensity of the fit peaks by the fraction of the total O 1s peak area, for the three O 1s fit peaks seen for $Ca_{0.8}Sr_{0.2}MnO_3$ taken under fixed reducing conditions of $T \approx 700$ °C and $p_{O_2} = 7.5 \times 10^{-4}$ mbar. The relative intensity of the peaks assumed to be surface species shows a decreasing trend with increasing excitation energy.

The species at higher binding energies correspond to less electron-rich oxygen species.[35] These are predominantly found at the sample surface, as indicated by their decreasing relative intensity at higher excitation energies, as seen in Fig. 5. Therefore, they constitute the perovskite lattice termination layer. The middle peak at approximately BE = 530.0 eV is attributed to electron-poor oxygen anions at the surface, which may include O_2^{2-}, O^-, and O_2^-.[35–37] The relative broadness of this peak may indicate that multiple different species with slightly different BEs are present. Finally, the peak at the largest BE (532.0 eV) corresponds to a more easily reduced species on the surface.[34,35]

Multiple XPS scans at different excitation energies were recorded, where Fig. 5 shows the relative area of the three peaks as a function of photon energy (depth).

Conclusions

In this work, $Ca_{0.8}Sr_{0.2}MnO_3$ was compared to $CaMnO_3$ with a focus on oxygen non-stoichiometry. The thermodynamic data were well described by a simple statistical model of defects, which indicated that the defects form clusters of the form $(Mn'_{Mn}V_O^{\cdot\cdot}Mn'_{Mn})^{\times}$. *In situ* X-ray spectroscopy of $Ca_{0.8}Sr_{0.2}MnO_3$ confirmed the partial reduction of Mn^{4+} to Mn^{3+}, depending on temperature and oxygen partial pressure. The TGA results show that $Ca_{0.8}Sr_{0.2}MnO_3$ has a number of advantages over $CaMnO_3$ when considering oxygen storage applications. Unlike $CaMnO_3$, $Ca_{0.8}Sr_{0.2}MnO_3$ appears to be robust against decomposition at high temperature and low partial pressure. $Ca_{0.8}Sr_{0.2}MnO_3$ is more easily reducible due to a slightly lower enthalpy change for the reduction reaction, and it shows faster reaction kinetics than the $CaMnO_3$ perovskite. The enhanced performance of $Ca_{0.8}Sr_{0.2}MnO_3$ can be understood by the addition of Sr improving the perovskite cubic structure, particularly for the reduced oxide. These properties make $Ca_{0.8}Sr_{0.2}MnO_3$ an excellent candidate material for chemical looping and it could be used to reach low oxygen partial pressures in oxygen pumping applications such as thermochemical air separation.

Experimental section

All perovskite materials have been prepared using a citric acid auto-combustion route described elsewhere,[38] with the full details given in the ESI.†

The perovskite phase formation was verified using X-ray diffractometry (XRD). X-Ray diffraction (XRD) experiments were carried out using a Siemens® D5000 XRD system equipped with a Cu-Kα X-ray tube (λ-CuKα = 1.540598 Å) and a secondary monochromator. Cell parameters were determined using the software MAUD *via* Rietveld refinement using data of $CaMnO_3$ in the literature as initial parameters.[39–41]

The composition of $Ca_{0.8}Sr_{0.2}MnO_3$ was confirmed *via* energy dispersive X-ray spectroscopy (EDX), performed using an Oxford INCA X-ray detector which is coupled to a Zeiss Ultra-55 SEM system at an acceleration voltage of 15 kV. The Zeiss Ultra-55 SEM was also used to take images of the powders after the kinetic analysis.

For thermal analysis, a thermobalance system by Netzsch (Model STA 449 F3 Jupiter) equipped with a silicon carbide furnace has been used, which can be operated in a temperature range from RT to 1550 °C with a maximum heating rate of 50 K min^{-1}. The powdered samples were placed on Pt sample holders mounted on ceramic pins. The concentration of oxygen in the TGA was controlled and measured using a combined pump and oxygen detector produced by Nernst Setnag. The oxygen pump was used to set the partial pressure of oxygen in an argon stream before it entered the TGA and the sensor was used to measure the partial pressure of oxygen in the gas leaving the TGA.

To measure the reaction kinetics, the samples were reduced under Ar 5.0 at 900 °C, cooled down under Ar to a lower temperature, and then subjected to a mixture of synthetic air and Ar 5.0 with $p_{O_2} = 0.16$ bar. Finally, the sample is brought to 500 °C in the same atmosphere to ensure full re-oxidation.

Near ambient pressure *in situ* X-ray photoelectron spectroscopy (NAP-XPS) and near-edge X-ray absorption (NEXAFS) measurements were performed at the ISISS beamline at the synchrotron X-ray source BESSY II, which are described by Starr *et al.*[42]

Measurements were carried out in oxygen atmospheres up to 1.0 mbar. The samples were heated to a temperature of up to 700 °C using an infrared laser. Temperature monitoring has been carried out using a pyrometer and type K thermocouple. The samples were cleaned inside the NAP-XPS at $T > 500$ °C under 1.0 mbar O_2 to remove carbonaceous species from the surface before the measurements. The photon energies were calibrated using the position of the Ca 2p XPS signals and their respective second order peaks. The O 1s XPS signal was observed to check for beam damage, and the sample position in the beam was changed if necessary. A Shirley background has been removed from each XPS scan, if necessary combined with a linear background function.

Acknowledgements

This work has received funding from the Helmholtz Association VH-VI-509, the DLR Programme Competition of Visions, and the project DÜSOL which is co-funded in the Klimaschutzwettbewerb "ErneuerbareEnergien.NRW" by the state of Northrhine-Westphalia, Germany, and the European EFRE fund. We would also like to thank the researchers and technical staff at the synchrotron X-Ray source BESSY II (Helmholtz-Zentrum Berlin für Materialien und Energie) for their kind support.

References

1 B. Moghtaderi, *Energy Fuels*, 2011, **26**, 15–40.
2 L. Nalbandian, A. Evdou and V. Zaspalis, *Int. J. Hydrogen Energy*, 2011, **36**, 6657–6670.
3 J. R. Scheffe, D. Weibel and A. Steinfeld, *Energy Fuels*, 2013, **27**, 4250–4257.
4 Q. Jiang, J. Tong, G. Zhou, Z. Jiang, Z. Li and C. Li, *Sol. Energ.*, 2014, **103**, 425–437.
5 E. Jerndal, T. Mattisson and A. Lyngfelt, *Chem. Eng. Res. Des.*, 2006, **84**, 795–806.
6 B. Moghtaderi, *Energy Fuels*, 2009, **24**, 190–198.
7 R. Siriwardane, H. Tian, G. Richards, T. Simonyi and J. Poston, *Energy Fuels*, 2009, **23**, 3885–3892.
8 M. Ezbiri, K. M. Allen, M. E. Gàlvez, R. Michalsky and A. Steinfeld, *ChemSusChem*, 2015, **8**, 1966–1971.
9 J. Hodges, S. Short, J. Jorgensen, X. Xiong, B. Dabrowski, S. Mini and C. Kimball, *J. Solid State Chem.*, 2000, **151**, 190–209.
10 J. Vieten, B. Bulfin, F. Call, M. Lange, M. Schmücker, A. Francke, M. Roeb and C. Sattler, *J. Mater. Chem. A*, 2016, **4**, 13652–13659.
11 E. Bakken, T. Norby and S. Stølen, *Solid State Ionics*, 2005, **176**, 217–223.
12 L. Rørmark, A. B. Mørch, K. Wiik, S. Stølen and T. Grande, *Chem. Mater.*, 2001, **13**, 4005–4013.
13 B. Dabrowski, O. Chmaissem, J. Mais, S. Kolesnik, J. Jorgensen and S. Short, *J. Solid State Chem.*, 2003, **170**, 154–164.
14 E. Bakken, J. Boerio-Goates, T. Grande, B. Hovde, T. Norby, L. Rørmark, R. Stevens and S. Stølen, *Solid State Ionics*, 2005, **176**, 2261–2267.
15 E. I. Leonidova, I. A. Leonidov, M. V. Patrakeev and V. L. Kozhevnikov, *J. Solid State Electrochem.*, 2011, **15**, 1071–1075.
16 M. Galvez, R. Jacot, J. Scheffe, T. Cooper, G. Patzke and A. Steinfeld, *Phys. Chem. Chem. Phys.*, 2015, **17**, 6629–6634.
17 B. Bulfin, L. Hoffmann, L. de Oliveira, N. Knoblauch, F. Call, M. Roeb, C. Sattler and M. Schmuecker, *Phys. Chem. Chem. Phys.*, 2016, **18**, 23147–23154.
18 B. Lee, K. M. Choi, H.-S. Ahn, S. Han, J. Lee, *et al.*, *Phys. Rev. Lett.*, 2007, **98**, 115503.
19 Y. Hao, C.-K. Yang and S. M. Haile, *Chem. Mater.*, 2014, **26**, 6073–6082.
20 M. Pishahang, Y. Larring, M. McCann and R. Bredesen, *Ind. Eng. Chem. Res.*, 2014, **53**, 10549–10556.
21 N. Galinsky, A. Mishra, J. Zhang and F. Li, *Appl. Energy*, 2015, **157**, 358–367.
22 T. Mattisson, A. Lyngfelt and H. Leion, *Int. J. Greenhouse Gas Control*, 2009, **3**, 11–19.
23 M. T. Curnan and J. R. Kitchin, *J. Phys. Chem. C*, 2014, **118**, 28776–28790.
24 A. Reller, J. Thomas, D. Jefferson and M. Uppal, *Proc. R. Soc. London, Ser. A*, 1984, 223–241.
25 S. Dubinin, N. Loshkareva, S. Teploukhov, Y. P. Sukhorukov, A. Balbashov, V. Arkhipov and V. Parkhomenko, *Phys. Solid State*, 2005, **47**, 1267–1272.
26 B. Wang, X. Xi and A. N. Cormack, *Chem. Mater.*, 2014, **26**, 3687–3692.
27 G. Murgida, V. Ferrari, M. V. Ganduglia-Pirovano and A. Llois, *Phys. Rev. B: Condens. Matter Mater. Phys.*, 2014, **90**, 115120.
28 A. H. McDaniel, E. C. Miller, D. Arifin, A. Ambrosini, E. N. Coker, R. O'Hayre, W. C. Chueh and J. Tong, *Energy Environ. Sci.*, 2013, **6**, 2424–2428.

29 A. Demont, S. Abanades and E. Beche, *J. Phys. Chem. C*, 2014, **118**, 12682–12692.
30 W. C. Chueh, C. Falter, M. Abbott, D. Scipio, P. Furler, S. M. Haile and A. Steinfeld, *Science*, 2010, **330**, 1797–1801.
31 M. Salmeron and R. Schlögl, *Surf. Sci. Rep.*, 2008, **63**, 169–199.
32 A. Saywell, G. Magnano, C. J. Satterley, L. M. Perdigão, A. J. Britton, N. Taleb, M. del Carmen Giménez-López, N. R. Champness, J. N. O'Shea and P. H. Beton, *Nat. Commun.*, 2010, **1**, 75.
33 M. Seah and W. Dench, *Surf. Interface Anal.*, 1979, **1**, 2–11.
34 E. J. Crumlin, E. Mutoro, Z. Liu, M. E. Grass, M. D. Biegalski, Y.-L. Lee, D. Morgan, H. M. Christen, H. Bluhm and Y. Shao-Horn, *Energy Environ. Sci.*, 2012, **5**, 6081–6088.
35 N. A. Merino, B. P. Barbero, P. Eloy and L. E. Cadús, *Appl. Surf. Sci.*, 2006, **253**, 1489–1493.
36 A. Bielański and J. Haber, *Catal. Rev.: Sci. Eng.*, 1979, **19**, 1–41.
37 J. Haber and B. Grzybowska, *J. Catal.*, 1973, **28**, 489–492.
38 A. E. Danks, S. R. Hall and Z. Schnepp, *Mater. Horiz.*, 2016, **3**(2), 91–112.
39 L. Lutterotti, D. Chateigner, S. Ferrari and J. Ricote, *Thin Solid Films*, 2004, **450**, 34–41.
40 L. Lutterotti, R. Vasin and H.-R. Wenk, *Powder Diffr.*, 2014, **29**, 76–84.
41 M. M. Jorge, A. C. dos Santos and M. Nunes, *Int. J. Inorg. Mater.*, 2001, **3**, 915–921.
42 D. Starr, Z. Liu, M. Hävecker, A. Knop-Gericke and H. Bluhm, *Chem. Soc. Rev.*, 2013, **42**, 5833–5857.